RESEARCH: Short Communication

Achieving 5.9% elastic strain in kilograms of metallic glasses: Nanoscopic strain engineering goes macro

Junsong Zhang [1], Yinong Liu [1,*], Hong Yang [1,*], Yang Ren [2], Lishan Cui [3], Daqiang Jiang [3], Zhigang Wu [1], Zhiyuan Ma [3], Fangmin Guo [3], Sam Bakhtiari [1], Fakhrodin Motazedian [1], Ju Li [4,*]

[1] Department of Mechanical Engineering, The University of Western Australia, Perth, WA 6009, Australia
[2] X-ray Science Division, Argonne National Laboratory, Argonne, IL 60439, USA
[3] Department of Materials Science and Engineering, China University of Petroleum-Beijing, Changping, Beijing 102249, China
[4] Department of Nuclear Science and Engineering and Department of Materials Science and Engineering, Massachusetts Institute of Technology, Cambridge, MA 02139, USA

The ideal elastic limit is the upper bound of the achievable strength and elastic strain of solids. However, the elastic strains that bulk materials can sustain are usually below 2%, due to the localization of inelastic deformations at the lattice scale. In this study, we achieved >5% elastic strain in bulk quantity of metallic glass, by exploiting the more uniform and smaller-magnitude atomic-scale lattice strains of martensitic transformation as a loading medium in a bulk metallic nanocomposite. The self-limiting nature of martensitic transformation helps to prevent lattice strain transfer that leads to the localization of deformation and damage. This lattice strain egalitarian strategy enables bulk metallic materials in kilogram-quantity to achieve near-ideal elastic limit. This concept is verified in a model in situ bulk amorphous (TiNiFe)-nanocrystalline (TiNi(Fe)) composite, in which the TiNiFe amorphous matrix exhibits a maximum tensile elastic strain of ~5.9%, which approaches its theoretical elastic limit. As a result, the model bulk composite possesses a large recoverable strain of ~7%, a maximum tensile strength of above 2 GPa, and a large elastic resilience of ~79.4 MJ/m^3. The recoverable strain and elastic resilience are unmatched by known high strength bulk metallic materials. This design concept opens new opportunities for the development of high-performance bulk materials and elastic strain engineering of the physiochemical properties of glasses.

Introduction

The ideal strength is the theoretical upper limit on a solid's ability to withstand load [1–5]. Whereas the ideal strength of a crystal is well defined [1–4], there is not yet a consensus on the proper atomistic definition of the ideal strength of a solid in glassy state [5–7], which comes with intrinsic structural heterogeneities. For crystals, the general guidance is $\sigma_{ideal} \approx 0.1E$ [1–4],

where σ_{ideal} is the ideal uniaxial tensile strength and E is Young's modulus. For metallic glasses, it has been suggested that $\sigma_{ideal} \approx 0.05E$ based on small-scale mechanical testing results [8–10]. This corresponds to ~5% elastic strain, which far exceeds the <2% elastic strains observed in most bulk metallic glass tests [6,11,12]. We note that ~5% tensile elastic strains (and corresponding deviatoric strains in 6-dimensional tensorial strain space) could lead to significant opportunities in elastic strain engineering [13,14] of the magnetic, chemical and transport properties of glasses. However, to date no one has been able to

---

* Corresponding authors.
    E-mail addresses: Liu, Y. (yinong.liu@uwa.edu.au), Yang, H. (hong.yang@uwa.edu.au), Li, J. (liju@mit.edu).

demonstrate elastic strains of such magnitude in macroscopic quantities of metallic glasses.

In crystalline materials, recent experiments have revealed ultra-high strengths and ultra-large stretching (true elastic strains) of interatomic bonds [15–17], which are intrinsic to the solids. For example, nanoscale diamond needles have been shown to exhibit a large elastic strain of 9% and a corresponding strength of ~98 GPa [15], a Cu nanowire was measured to have a large elastic strain of 7.2% [16], and an Al_2O_3 nanowire was measured to exhibit 8.5% elastic strain [17]. However, these near-ideal true elastic strains are all achieved in isolated nanometer-size samples, which are largely defect free. Such properties are usually not accessible in bulk materials due to the presence of structural defects extrinsic to the interatomic bonding in the solids [18–21], such as dislocations and lattice cracks. These structural defects cause premature failure before the full strength potential of the interatomic bonding can be realized.

To overcome this, various strengthening techniques have been developed for bulk materials, such as solid solution strengthening, forest dislocation strengthening, grain boundary strengthening, and precipitation strengthening. The underlying philosophy of these approaches is to hinder activities of extended defects, e.g. dislocation motion. Despite all these efforts, bulk crystalline metals seldom show elastic strains above ~1.3% [18–28].

Design concept

Rethinking of the failure mechanisms of bulk materials, it is easy to understand that all macroscopic failures of bulk materials originate from the accumulation of local structural damages within the lattice. Microscopically, in coarse-grain crystalline materials, dislocation motion generates large inelastic strains that can be expressed by nb/d, where n is the number of dislocations that have passed, b is the Burgers vector, and d is the interplanar spacing of the slip plane. Generally $b/d \geq 100\%$, i.e. plastic deformation by dislocation motion is quantized by $b/d \geq 100\%$, which is grossly excessive relative to the intrinsic elastic strain limit of the interatomic bonds (typically up to 10%). Furthermore, since n is unrestricted, dislocation slip is intrinsically not self-limiting, i.e. the same Frank-Read source can emit hundreds of dislocations that pass the same spot on the same slip plane repeatedly. This non-self-limiting behavior creates excessive stress concentrations in front of the pileup, and jeopardizes the chance for achieving true elasticity in the body that causes the pileup. Indeed, the stress generated inside the obstacle is similar to that of a mode-II or mode-III shear-crack singularity. For bulk materials with sub-micron grain sizes or heavily defected matrices, e.g., after severe plastic deformation, such uncontrolled supply of dislocations and excessively high dislocation pileups will not occur. In this case mechanical failure may take the form of grain boundary sliding, which is yet another form of excessive local damage at the lattice scale.

In amorphous materials, cooperative local rearrangement of atoms may occur in response to an applied load at relatively low levels of global deformation, known as the shear transformation zones (STZ) [29,30]. STZs are generally very small in volume (typically ~1 nm³) and incur relatively low lattice distortions, or

stretching between pairs of atoms, typically on the order of several percent. They are self-catalytic, i.e. they tend to trigger similar activities within their vicinities due to a strain-energy correlation effect [31]. With increased deformation, neighboring STZs coalesce to form shear bands, which incur much greater local deformations, e.g. up to ~1000% [32].

Fig. 1(a) illustrates the most common forms of mechanical failure of bulk materials, including dislocation slip (I), lattice cracking (II), grain boundary sliding (III) and shear band sliding in amorphous alloys (IV). Local structural damages are always highly concentrated with extremely large "atomistic" strains. For example, during plastic deformation via dislocation slip, which may be macroscopically uniform and insignificant, the lattice deformation after one single dislocation passed is ≥100%, or ~10,000% for a slip band (illustration (I)) [33,34]. For a lattice crack of 1 nm width, which is totally insignificant macroscopically, the lattice opening is approximately three times of the interatomic distance, or ~300% equivalent lattice strain (or ~300,000% for a 1 μm crack), as illustrated in (II). For nanograined metals with grain sizes below ~10 nm, the local deformation caused by the grain boundary sliding can be up to ~1000% (illustration (III)) [35]. In amorphous alloys, the local deformation at a shear band can be easily ~1000%, as illustrated in (IV) [32].

Realization of the occurrence of such excessively large local inelastic strains invites us to take a new look at our approach to strengthening materials. The occurrence of such excessively large "atomistic" strains at even the smallest global deformation implies excessive lattice strain concentration, i.e. when local damages occur within the lattice, the defect-free parts act as a strain transfer medium to concentrate the applied global (macroscopic) strain to the sites of the local damages. Therefore, the key to achieving the full potential of ideal elastic limit, or ideal strength, in a large material mass is to suppress or to eliminate strain transfer and concentration to prevent strain localization and damage accumulation.

Suppression of lattice strain concentration can be achieved by using martensitic transformation found in some metal alloys. Martensitic transformation differs from all the lattice inelasticity mechanisms presented above in one unique aspect, in that it is *self-limiting*. It is a diffusionless collective crystal lattice distortion process with a uniform lattice strain between *every* two adjacent atoms, i.e. highly "egalitarian". The magnitude of the atomic-level inelastic strain ranges from several percent to more than ten percent (e.g. ~10% in TiNi) [36,37], which is conveniently comparable in magnitude to the ideal elastic strain limits of most solids. In other words, there is a good "strain-matching" in magnitude between the inelastic crystallographic strain of the phase transformation (~10% in TiNi) and the elastic strain limits (~10% in crystals and ~5% in metallic glasses) at the atomistic level. This is in clear contrast to the "quantized" minimum lattice strains of dislocation motion (nb/d) and lattice cracking of >100% at the atomistic level. Fig. 1(b) shows a schematic of the atomic-level lattice strains of a martensitic transformation. This implies that it is possible to create a bi-metal composite, in which martensitic transformation (B) is used as a strain "equalizer" to uniformly partition the global strain into millions of smaller and equal parts of "atomistic strains" (both pseudo-elastic and true elastic), as illustrated in Fig. 1(c).
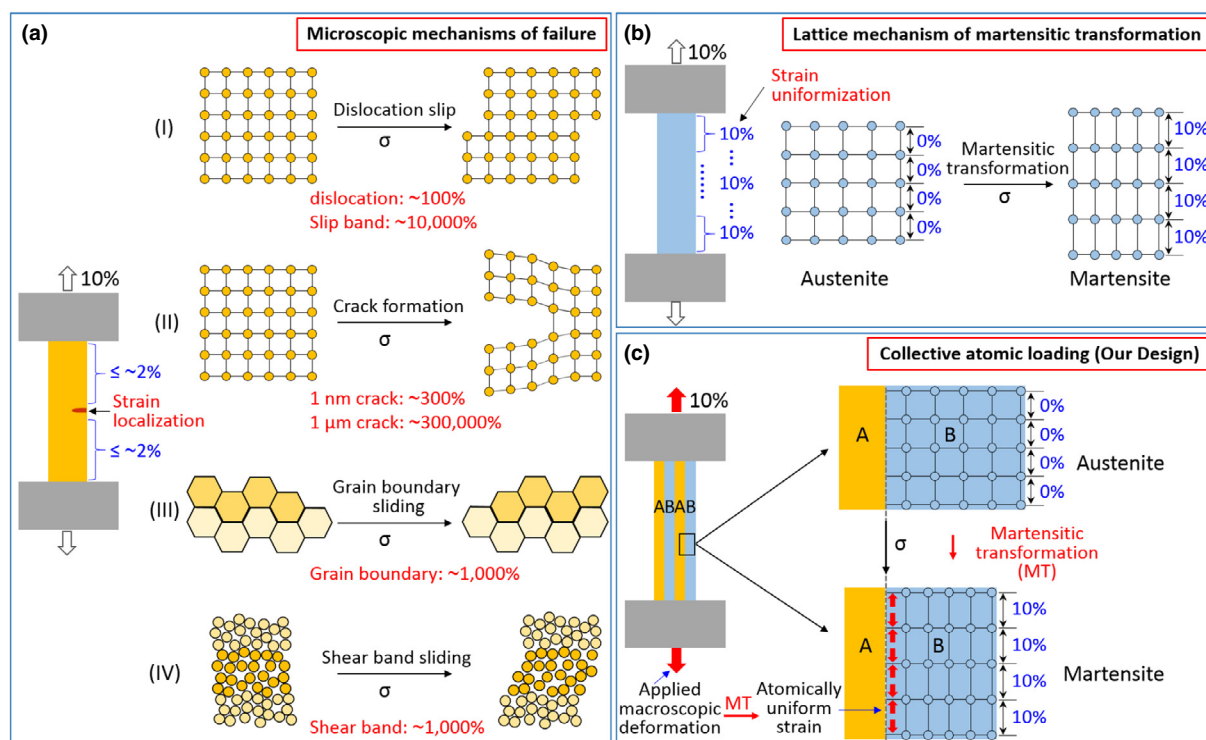
FIGURE 1

Schematic of the design concept. (a) Microscopic mechanisms of failure of bulk materials, including (I) dislocation slip, (II) lattice cracking, (III) grain boundary sliding, as observed in nanograined metal alloys, and (IV) shear band sliding, as observed in amorphous metal alloys. The schematics illustrate the excessively large localized lattice damages. (b) Martensitic transformation and its microscopic mechanism of uniform lattice distortion (e.g. ~10% in TiNi), and its implication of uniform distribution of the global strain, preventing deformation localization at the lattice scale. (c) Schematic of our design concept, which entails a composited structure of a conventional metal alloy (a) with a martensitic transformation alloy (b), which upon loading divides the applied global (macroscopic) strain into millions of small compartmentalized lattice strains by its martensitic transformation, thus preventing strain transfer by the elastic lattice of alloy A to cause strain localization at the lattice scale.

The equalization and distribution of the global deformation into the lattice level by the martensitic transformation also imply that the load is transferred more uniformly between the two bodies at the atomic level along their interfaces, i.e. martenstic transformation enabled collective atomic loading. It is obvious that this mechanism of collective atomic loading requires intimate interaction of the two components (pseudoelasticity via transformation and true elasticity) at the nanometric scale. An optimized microstructure design is presented in Fig. S1(d) in the Supplementary Information, in comparison with other configurations based on size and spacing of the martensitic transformation inclusion phase in the composite (Fig. S1). The optimal configuration features a high density (fine spacing) of martensitic transformation alloy nanoinclusions (fine size) uniformly distributed within a continuous conventional bulk metal matrix (glassy or crystalline). The characteristic conditions of these structures are summarized in Table S1, in which (d) is the optimal design.

Results and discussion

Based on this concept, we designed a series of in situ bulk nanocomposites of TiNiX consisting of crystalline nanodomains embedded in an amorphous matrix. In these composites, the crystalline inclusions and the amorphous matrix are of the same chemical composition (though not a compulsory condition), i.e.

they are structural composites. This design is supported by the fact that TiNi-based shape memory alloys are easily amorphized by severe plastic deformation [38,39], thus allowing good design flexibility for the volume fraction and size of the crystalline nanoinclusions via crystallization heat treatment of the amorphous matrix. In addition, such in situ solid-state-amorphsiza tion-and-crystallization alloy system assures good interfacial cohesion between the inclusions and the matrix. Fig. S2 presents the condition of the TiNi(Fe) crystalline wire before the final amorphisation cold deformation, including its structure, transformation behavior and mechanical behavior. Fig. S3 presents the amorphous TiNiFe alloy obtained after the severe plastic deformation and its crystallization behavior.

Fig. 2 shows the microstructures of two partially crystallized samples after heat treatment at 300 °C (Fig. 2(a)) and 295 °C (Fig. 2(b)) for 10 min. The samples contain high-densities of equiaxial nano-sized grains dispersed in an amorphous matrix. The average size of the nanograins are 9.7 nm in the 300 °C annealed sample and 9.4 nm in the 295 °C annealed sample. Statistical information on the grain size distribution is given in Fig. S4. The volume fractions of the amorphous matrix are estimated, based on the size of the crystallization exothermic peak relative to the fully amorphous sample (Fig. S5), to be 39% in the 300 °C annealed sample and 49% in the 295 °C annealed sample. The selected-area electron diffraction (SAED) patterns
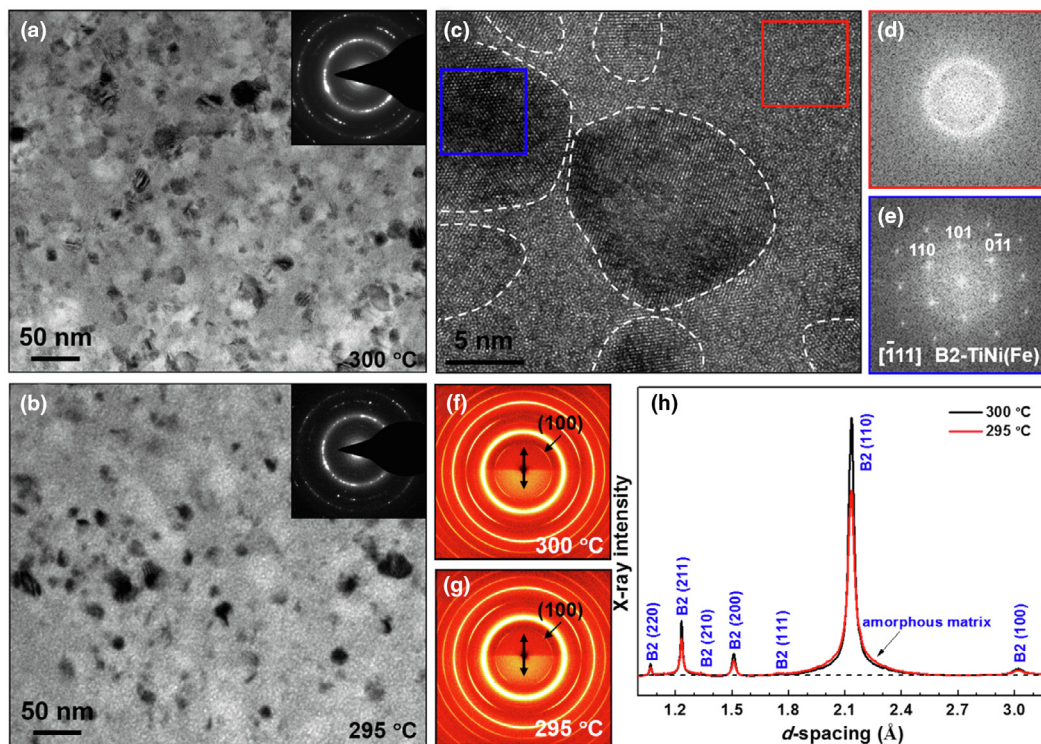
FIGURE 2

Microstructures of the in situ amorphous-nanocrystalline TiNiFe composites. (a) TEM bright-field image of a sample annealed at 300 °C for 10 min. (b) TEM bright-field image of a sample annealed at 295 °C for 10 min. The insets in (a) and (b) show their corresponding SAED patterns. (c) HRTEM image of the 300 °C annealed sample. (d) FFT pattern of the amorphous region (the red frame) identified in (c). (e) FFT pattern of the nanocrystalline region (the blue frame) identified in (c). (f) Two-dimensional HE-XRD pattern of the 300 °C annealed sample. (g) Two-dimensional HE-XRD pattern of the 295 °C annealed sample. The double arrows in (f) and (g) indicate the wire axial direction. (h) One-dimensional HE-XRD spectrums of the two samples obtained by 360° integration along the azimuth circle of the 2D HE-XRD patterns.

shown in the insets in Fig. 2(a) and Fig. 2(b) reveal the amorphous matrix and several discontinuous crystalline rings corresponding to the B2-TiNi(Fe) phase.

Fig. 2(c) shows a high-resolution transmission electron microscopic (HRTEM) image of the 300 °C annealed sample (the 295 °C annealed sample is shown in Fig. S4(c)). Fast Fourier Transform (FFT) patterns from the amorphous matrix and a nanocrystalline region are shown in Fig. 2(d) and (e) (also in Fig. S4(e) and (d)), respectively, confirming their respective structures. Energy-dispersive X-ray spectroscopic analysis (Fig. S6) confirms the uniform composition of the annealed samples. Fig. 2(f) and (g) present 2D synchrotron high-energy X-ray diffraction (HE-XRD) patterns of the two samples. The B2-TiNi (Fe) nanocrystalline grains have a clear preferential orientation in both samples, with their [1 0 0] direction oriented at ±50° from the wire axial direction (indicated by the double arrow). Further details are presented in Fig. S7. Fig. 2(h) shows 1D HE-XRD patterns of the two samples obtained by 360° integration along the Debye circle of the respective 2D HE-XRD patterns.

The mechanical properties of the in situ amorphous-nanocrystalline composites were studied by tensile testing, and the engineering stress–strain curves are shown in Fig. 3(a) (true stress–strain curves are presented in Fig. S8). The 300 °C annealed sample exhibits a tensile yield strength of ~1.60 GPa, an ultimate tensile strength of ~2.02 GPa, a recoverable strain of ~7.0%, and an elastic resilience (recoverable elastic energy) of ~79.4 MJ/m^3.

The 295 °C annealed sample exhibits a tensile yield strength of ~1.70 GPa, an ultimate tensile strength of ~2.25 GPa, a recoverable strain of ~5.5%, and an elastic resilience of ~73.5 MJ/m^3. The large strains of the composites recovered upon unloading imply that the amorphous matrices in our composites have contained large elastic strains.

Fig. 3(b) shows a comparison of the recoverable elastic strains and ultimate strengths of our composites against those of other high strength bulk metallic materials reported in the literature (a comparison of yield strength is presented in Fig. S9(a)) [11,18,20–28,40–47]. Fig. 3(c) (and Fig. S9(b)) compares the elastic resilience between the same materials [11,18,20–28,40–47]. It is apparent that our amorphous-nanocrystalline composites far outperform other materials on recoverable elastic strain and recoverable elastic energy density. The only class of materials having similar or larger recoverable strains (typically 2–10%) are shape memory alloys, which have much lower strengths (typically <1 GPa) (Fig. S10(a) and (b)) and elastic resiliencies (typically <30 MJ/m^3) (Fig. S10(c) and (d)). The high recoverable strains and elastic resiliencies of our composites imply that they are suited not only for high strength applications, but also as functional materials for actuation and mechanical energy storage applications.

To uncover the microscopic mechanisms of the deformation of the amorphous-nanocrystalline composites, in situ synchrotron HE-XRD measurements were performed during tensile
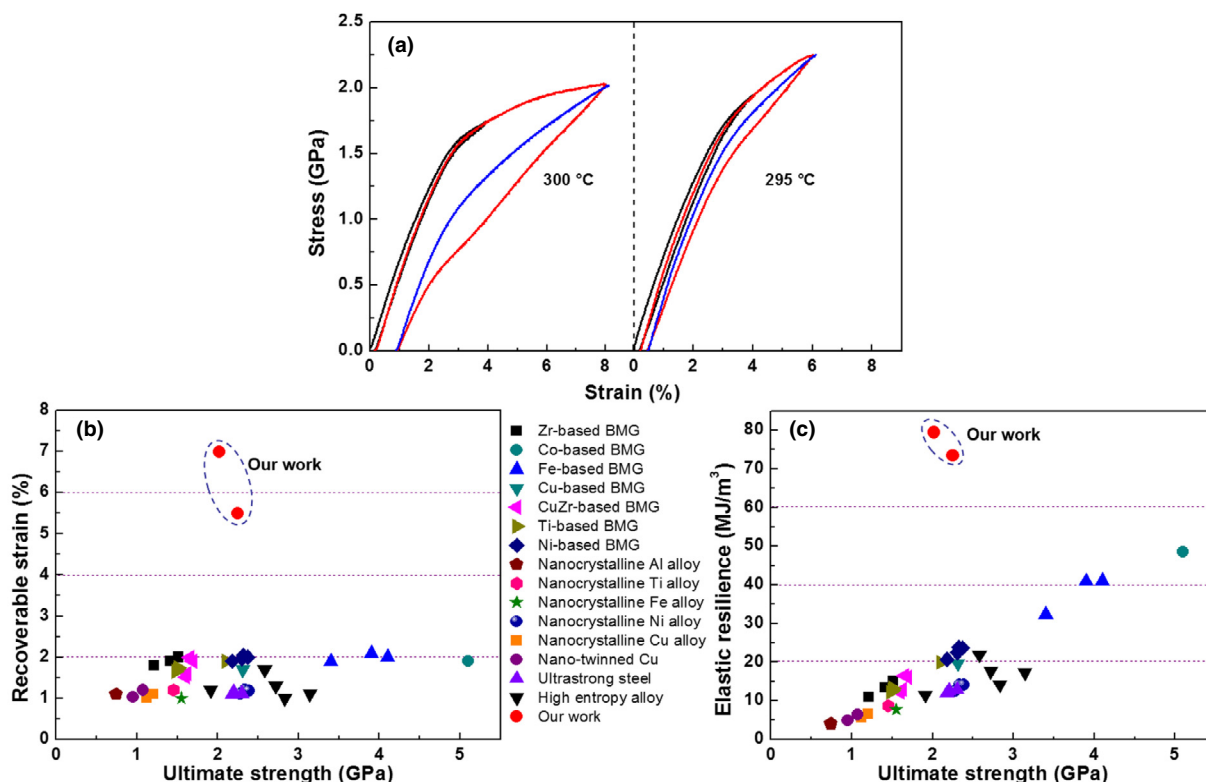
FIGURE 3

Mechanical behavior of the in situ amorphous-nanocrystalline composites. (a) Engineering tensile stress–strain curves of the 300 °C and 295 °C annealed samples. (b) Comparison of the recoverable strain and ultimate strength of our composites with those of other high strength bulk metallic materials. (c) Comparison of the elastic resilience and ultimate strength of the same materials as in (b). These existing high strength bulk metallic materials include Zr-based bulk metallic glass (BMG) [40], Co-based BMG [41], Fe-based BMG [42], Cu-based BMG [11,43], CuZr-based BMG [44,45], Ti-based BMG [46], Ni-based BMG [47], nanocrystalline Al alloy [22], nanocrystalline Ti alloy [23], nanocrystalline Fe alloy [24], nanocrystalline Ni alloy [25], nanocrystalline Cu alloy [26], nano-twinned Cu [21], ultra-strong steel [18,27], and high entropy alloy [20,28].

deformation. Fig. 4 presents the analysis for the 300 °C annealed sample (further information is given in Figs. S11 and S12). Fig. 4 (a) presents 1D HE-XRD patterns of the sample at various stages of deformation in the loading direction. It is seen that the nanocrystalline B2-TiNi(Fe) phase (e.g. as represented by B2 (2 1 1) diffraction) underwent an initial elastic deformation and then a transformation to B19′ martensite during the tensile deformation. Fig. 4(b) plots the evolution of the relative integrated diffraction peak intensities of B2 (1 0 0) and B19′ (0 0 1) on the applied strain (also in Fig. S11) associated with the phase transformation.

Fig. 4(c) shows the evolutions of the microscopic strains of the amorphous matrix and the nanocrystalline B2-TiNi(Fe) phase during the deformation. The stage at <2.8% global strain corresponds to the initial elastic deformation of the composite. The leveling of the B2 (2 1 1) lattice strain corresponds to the macroscopic yielding (Fig. 3(a) and the inset in Fig. 4(c)) of the composite in association of the stress induced martensitic transformation (Fig. 4(b)). In comparison, the elastic strain of the amorphous matrix increased throughout the stages of the initial elastic deformation and the stress-induced martensitic transformation of the nanocrystalline phase, reaching ∼5.9% at the end of the tensile deformation (∼8.8% macroscopic strain).

There is a mismatch in magnitude between the crystallographic strain of the martensitic transformation in the crystalline nanodomains and the elastic strain of the amorphous matrix. Consequently, upon deformation, plastic deformation will occur in the amorphous matrix, which in turn causes residual stresses within the composite after a complete pseudoelastic deformation cycle. The evidence is seen in Figs. S12(b), (c), (e) and (f). Upon unloading, the austenite B2-TiNi(Fe) phase underwent a full reverse transformation from the stress-induced B19′ martensite to the B2 austenite phase. After unloading, the B2-TiNi(Fe) nanocrystalline phase sustained an elastic tensile strain (Fig. S12(d)), whereas the amorphous matrix sustained an elastic compressive strain. These microscopic elastic strains increased with increasing the macroscopic tensile cycle strain (Fig. S12 (d)). The presence of the microscopic residual lattice strain after the deformation cycle implies that plastic deformation has occurred in the amorphous matrix during the deformation cycle, which caused the macroscopic residual strain of the composite after unloading. Due to the residual elastic tensile strain in the B2-TiNi(Fe) nanocrystalline phase after unloading, the critical stress for the stress-induced martensitic transformation will decrease, which leads to a reduction of macroscopic yield stress in the subsequent tensile deformation cycles (Fig. 3(a)).
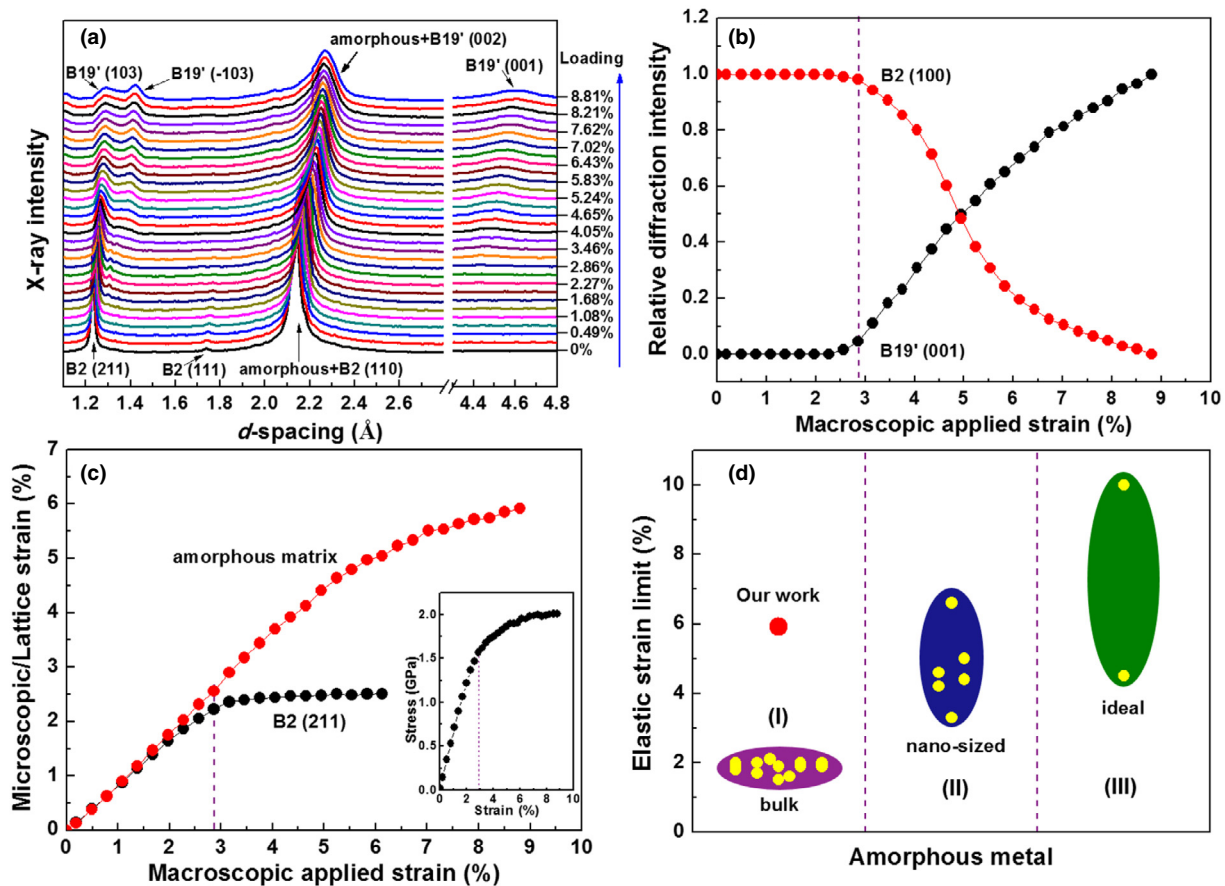
FIGURE 4

In situ synchrotron HE-XRD analysis of the microscopic mechanisms of deformation of the amorphous-nanocrystalline composites. (a) HE-XRD spectrums of the 300 °C annealed sample collected at various stages during tensile deformation. The spectra were integrated within ±5° along the Derby circle in the loading direction. (b) Evolution of the relative integrated peak intensities of B2 (1 0 0) and B19′ (0 0 1) diffractions during the tensile deformation. The relative intensity is defined as the ratio of the integrated area of a peak to that at the strain-free state for the B2 phase (100% B2) and to that at the maximum applied strain for the B19′ phase (100% B19′). (c) Evolution of the microscopic strains of amorphous matrix and the nanocrystalline B2 (2 1 1) along the loading direction as functions of the macroscopic applied strain. The inset shows the corresponding macroscopic stress–strain curve. (d) Comparison of the elastic strain limit of the amorphous matrix in our composite with those of bulk metallic glasses (cell I) [11,40–47], nano-sized amorphous metals (cell II) [8,9,48], and the ideal amorphous materials (cell III) [5,8].

Fig. 4(d) presents a comparison of the elastic strains of the amorphous matrix in our composite with those of bulk [11,40–47] and nano-sized [8,9,48] amorphous metals, and the ideal values [5,8] estimated using molecular dynamics simulation method. The ultra-large elastic strain (5.9%) of the amorphous matrix in our composite is significantly higher than those of BMG materials [11,40–47], comparable to the elastic strain limits of nano-sized amorphous metals [8,9,48], and approaching the ideal theoretical values [7] of amorphous metals [5,8]. It also implies a tensile strength exceeding ~5.3 GPa, estimated using $E = 90$ GPa for the amorphous matrix determined from the applied stress – microscopic stain curves shown in Fig. S13. The large elastic strain of the amorphous matrix contributes to the large recoverable strain of the composite.

The achievement of the 5.9% elastic strain in the TiNiFe amorphous matrix, which is approximately three times of the elastic strains of stand-alone bulk amorphous TiNiFe alloys (Figs. S3(c) and S13), is attributed to the effect of lattice strain equalization and distribution of the phase-transforming TiNi (Fe) nanocrystalline domains highly dispersed within the matrix.

Upon loading, the stress-induced martensitic transformation in the nanocrystalline domains helps to divide the applied global (macroscopic) strain into small and uniform crystallographic and true elastic strains at the atomic level, and to transfer the load collectively between adjacent atoms in the two phases across the interface. The crystallographic strain of the martensitic transformation is self-limiting, i.e. with a finite value, and small in magnitude at the atomic level, in contrast to the excessively large strains at the atomic-level (nb/d) of dislocation slip.

The essence of the effect of the martensitic transformation is to regulate the magnitude of local lattice distortion within the amorphous matrix by its crystallographic lattice strains. The lattice distortions, or stretching between pairs of atoms, of the local atomic rearrangement volumes within the amorphous matrix are generally very small and martensitic transformation in the crystalline domains may have little restriction to their formation. However, the coalescence of these local atomic rearrangement volumes into shear bands will rapidly raise the local lattice distortions to far greater values, on the order of 1000%. Then the finite crystallographic strains of the martensite in the crystalline

domains are effective in suppressing this coalescence process and nucleation of shear bands, thus prevent deformation localization and pre-mature failure of the amorphous matrix. This allows the amorphous matrix to continue to load to higher stress levels and achieve its intrinsic potential in elastic strain and strength.

To further verify this hypothesis, several additional experiments have been conducted. First we tested samples in which the martensitic transformation in the nanocrystalline TiNi(Fe) domains is suppressed by decreasing the phase transformation temperature (Fig. S14) or increasing the testing temperature (Fig. S15). This allows the nanocrystalline domains to deform by dislocation slip. In this case the composites become brittle (Figs. S14(b), S15(b), (c), and (d)), and the maximum elastic strains achieved in the amorphous matrix are reduced to below 2.8% (Fig. S15(c) and (d)). In a second experiment we reduced the volume fraction of the embedded nanocrystalline phase by lowering the annealing temperature (Fig. S16). In this case the composites also become brittle with reduced elastic strains (Fig. S16(b)), since damage and shear-localization, once started in the metallic glass, cannot be halted easily [7].

It is obvious that this mechanism of lattice strain equalization and transfer requires intimate contact between the phase transforming nanocrystalline domains and the amorphous matrix. For maximum synergy between the two, an optimum microstructure can be anticipated. This may include an optimum volume fraction, size and morphology of the nanocrystalline domains. Too small a volume fraction of the crystalline domains will not be sufficient to impose the equalized crystallographic strains of the martensite to the amorphous matrix. On the other hand, too large of it reduces the strength of the composite, which is largely from the amorphous matrix. The strain transfer is an interface effect, thus a high total interface is desirable. Too large size of the crystalline domains reduce the total interface area but too small of the size reduces the mechanical potency of the martensite in transmitting the lattice strains to the matrix. In addition, high dispersion and uniformity of distribution is also desirable. What the optimal size and volume fraction are will require extensive experimentation and possibly theoretical analysis using density functional theory calculation or molecular dynamic simulations. However, the control of the size and volume fraction of the crystalline domains can be easily achieved by controlling the in situ crystallization heat treatment process, as demonstrated in Figs. 2 and S4.

We note that much work has been done in the past decades to create composites consisting of martensitic transformation phases embedded in bulk materials [44,45,49,50]. However, the aims in the past had been mostly to utilize the martensitic transformation to improve the plasticity and toughness of the matrix, e.g. *transformation induced plasticity* in steels [49], Ti alloys [50], and bulk metallic glasses [44,45]. This is largely based on the concept of stress relaxation at crack tips by the large inelastic deformation of the martensitic transformation. This work presents a new concept of *transformation induced strength and elastic resilience*, with potential application in elastic strain engineering [13,14,51] of physiochemical properties at the kilogram scale. The atomistic mechanism of the transformation induced strength is the "collective atomic loading" at the amorphous-crystalline interface. This concept requires high density, small

size and small inter-domain spacing for the martensitic transforming nanocrystalline domains. Composite structures of low domain density and large spacing of the martensitic transformation component (Fig. S1(a) and (c)) are unable to achieve effective atomically uniform load transfer [44,45]. The design of Fig. S1(b) is effective in achieving collective atomic loading, but unable to offer high strength due to its low volume fraction of the matrix.

Conclusions

This work presents a new concept of martensitic transformation enabled near-ideal strength based on the atomistic mechanism of "collective atomic loading" at the lattice level. By creating an in situ amorphous matrix-martensitic transforming nanocrystalline composite through partial crystallization anneal of an amorphous alloy, we have demonstrated a feasible mechanism and design strategy for achieving near-ideal elastic strain and near-ideal strength of amorphous materials in bulk quantities. The TiNiFe in situ composites achieved an elastic strain of ~5.9% in the amorphous matrix, a maximum strength of above 2 GPa, a recoverable elastic strain of ~7.0%, and an elastic resilience of ~79.4 MJ/m^3. Elastic strains above 5% are expected to be able to cause significant changes in physiochemical properties [14] of crystalline and glassy solids, such as electronic, magnetic, superconducting, optical, phononic, and catalytic properties [13]. It is also noted that the kilogram-scale metallic glass matrix still maintains its spatial percolation, thus these altered physiochemical properties can be truly macroscopic in spatial extent.

Methods

A 1.5 kg alloy ingot with a nominal composition of Ti$_{50}$Ni$_{47}$Fe$_3$ (at.%) was prepared by arc melting in a water-cooled copper hearth in an argon atmosphere. Commercial purity Ti (99.99 wt.%), Ni (99.99 wt.%) and Fe (99.99 wt.%) were used as raw materials. The button shaped ingot was re-melted six times in the furnace to obtain chemical composition homogeneity. The ingot was hot-forged at 850 °C into a rod of 12 mm in diameter and further hot-drawn at 750 °C into a wire of 2 mm in diameter. Then the hot-drawn wire was cold-drawn into a thin wire of 0.9 mm in diameter at room temperature with intermediate annealing at 750 °C for 0.6 ks in air. The ϕ0.9 mm wire was then cold-drawn to further reduce the diameter to 0.24 mm, producing an area reduction of 92.9%. The severe cold wire drawing induced full amorphization of the alloy. The test samples were cut from the cold-drawn ϕ0.24 mm wire and subsequently annealed at different temperatures (290 °C, 295 °C, and 300 °C) for 0.6 ks to cause partial crystallization to form the designed in situ amorphous-nanocrystalline composite structures.

The microstructure and chemical composition of the composite wires were analyzed using a FEI Tecnai G2 F20 transmission electron microscope (TEM) and a FEI Titan G2 80–200 TEM equipped with an energy dispersive X-ray spectrometer (EDS). Differential scanning calorimetry (DSC) measurements were conducted using a TA INST2910 differential scanning calorimeter with a heating/cooling rate of 10 °C/min for transformation behavior characterization and 20 °C/min for crystallization treat-

ment. Tensile tests were performed using an Instron universal mechanical testing machine at a strain rate of $5 \times 10^{-4} \, \mathrm{s}^{-1}$.

Synchrotron high-energy X-ray diffraction (HE-XRD) measurements were performed during in situ tensile deformation on Beamline 11-ID-C at the Advanced Photon Source, Argonne National Laboratory, USA. High-energy X-rays of 105.8 keV in energy level, 0.1173 Å in wavelength and $0.5 \times 0.5 \, \mathrm{mm}^2$ in beam size were diffracted in transmission geometry towards a Perkin-Elmer large area detector placed behind the sample to obtain two-dimensional (2D) HE-XRD diffraction patterns. Gaussian fit was employed to determine the position and area of a diffraction peak. The lattice strain for a particular set of crystal planes is calculated as $(d_{hkl} - d_{hkl}^{\circ})/d_{hkl}^{\circ}$, where d_{hkl}° is the "unstressed" lattice d-spacing (i.e. the peak position at zero applied stress). The errors of the lattice strain measurements and the relative peak intensity measurements were estimated to be less than 0.05% and 0.02, respectively. To evaluate the microscopic strains of the amorphous matrix, the diffraction pattern of the amorphous matrix was first obtained by subtracting from the total diffraction the diffraction pattern of the fully crystallized sample (having the same texture as the partially crystallized sample) using the Generalized Structure Analysis Software (GSAS) [52]. The first (main) scattering hump of the amorphous phase was first curve-fitted with the Voigt function to determine its peak position, and the position shift is then used to calculate the elastic strain relative to the stress-free state, as for a crystalline phase, as $(q_0 - q)/q$, where q_0 is the position of the first peak in the reciprocal space under zero applied stress [53,54]. The error in the microscopic elastic strain measurement of the amorphous structure was estimated to be less than 0.25%.

CRediT authorship contribution statement

Junsong Zhang: Conceptualization, Methodology, Validation, Formal analysis, Investigation, Data curation, Writing - original draft, Writing - review & editing, Supervision. **Yinong Liu:** Conceptualization, Methodology, Validation, Formal analysis, Writing - review & editing, Supervision, Project administration, Resources, Funding acquisition. **Hong Yang:** Conceptualization, Methodology, Validation, Writing - review & editing, Supervision, Project administration, Funding acquisition. **Yang Ren:** Validation, Formal analysis, Investigation, Resources. **Lishan Cui:** Formal analysis, Investigation, Resources. **Daqiang Jiang:** Formal analysis, Investigation. **Zhigang Wu:** Formal analysis, Investigation. **Zhiyuan Ma:** Formal analysis, Investigation. **Fangmin Guo:** Formal analysis, Investigation. **Sam Bakhtiari:** Formal analysis, Investigation. **Fakhrodin Motazedian:** Formal analysis, Investigation. **Ju Li:** Conceptualization, Methodology, Formal analysis, Writing - review & editing, Supervision.

Acknowledgements

Author contributions

Y. Liu, J. Zhang and H. Yang developed the original concept and materials design of the research, and supervised the project. J. Li contributed in the development of the scientific concept and data analysis of the project. J. Zhang carried out materials preparation and mechanical property testing, and conducted most data analysis. L. Cui and D. Jiang contributed in materials processing and mechanical testing. Y. Ren designed and supervised the synchrotron experiments. Z. Ma and F. Guo carried out the synchrotron experiments. Z. Wu, S. Bakhtiari and F. Motazedian contributed in TEM, XRD and DSC analyses. J. Zhang, Y. Liu, H. Yang and J. Li prepared the manuscript.

Appendix A. Supplementary data

Supplementary data to this article can be found online at https://doi.org/10.1016/j.mattod.2020.02.020.

References

[1] J. Frenkel, Z. Phys. 37 (1926) 572–609.
[2] T. Zhu, J. Li, Prog. Mater. Sci. 55 (2010) 710–757.
[3] F. Liu, P.M. Ming, J. Li, Phys. Rev. B 76 (2007) 064120.
[4] C. Lee et al., Science 321 (2008) 385–388.
[5] Y.Q. Cheng, E. Ma, Acta Mater. 59 (2011) 1800–1807.
[6] M.M. Trexler, N.N. Thadhani, Prog. Mater. Sci. 55 (2010) 759–839.
[7] P.Y. Zhao, J. Li, Y.Z. Wang, Acta Mater. 73 (2014) 149–166.
[8] L. Tian et al., Nat. Commun. 3 (2012) 609.
[9] Q. Deng et al., Acta Mater. 59 (2011) 6511–6518.
[10] C.C. Wang et al., Acta Mater. 60 (2012) 5370–5379.
[11] W.H. Wang, J. Appl. Phys. 99 (2006) 093506.
[12] W.L. Johnson, K. Samwer, Phys. Rev. Lett. 95 (2005) 195501.
[13] J. Li, Z.W. Shan, E. Ma, MRS Bull. 39 (2014) 108–117.
[14] Z. Shi et al., Proc. Natl. Acad. Sci. USA 116 (2019) 4117–4122.
[15] A. Banerjee et al., Science 360 (2018) 300–302.
[16] Y. Yue et al., Nano Lett. 11 (2011) 3151–3155.
[17] S. Wang et al., Nanotechnology 24 (2013) 285703.
[18] S. Jiang et al., Nature 544 (2017) 460–464.
[19] T. Yang et al., Science 362 (2018) 933–937.
[20] Y.J. Liang et al., Nat. Commun. 9 (2018) 4063.
[21] L. Lu et al., Science 323 (2009) 607–610.
[22] K.M. Youssef et al., Scr. Mater. 54 (2006) 251–256.
[23] B.B. Sun et al., Acta Mater. 54 (2006) 1349–1357.
[24] X.H. Chen et al., Scr. Mater. 52 (2005) 1039–1044.
[25] H. Li, F. Ebrahimi, Acta Mater. 54 (2006) 2877–2886.
[26] K. Youssef et al., Acta Mater. 59 (2011) 5758–5764.
[27] B.B. He et al., Science 357 (2017) 1029–1032.
[28] Y.J. Zhou et al., Appl. Phys. lett. 90 (2007) 181904.
[29] Y. Fan, T. Iwashita, T. Egami, Nat. Commun. 5 (2014) 5083.
[30] M. Fan et al., Phys. Rev. E 95 (2017) 022611.
[31] S.S. Jiang et al., Int. J. Plast. 125 (2020) 52–62.
[32] S. Pauly et al., Acta Mater. 58 (2010) 4883–4890.
[33] S. Ogata, J. Li, S. Yip, Science 298 (2002) 807–811.
[34] J.C. Fisher, E.W. Hart, R.H. Pry, Phys. Rev. 87 (1952) 958–961.

[35] J. Schiøtz, F.D.D. Tolla, K.W. Jacobsen, Nature 391 (1998) 561–563.
[36] K. Otsuka, X. Ren, Prog. Mater. Sci. 50 (2005) 511–678.
[37] S. Hao et al., Science 339 (2013) 1191–1194.
[38] C. Yu et al., Acta Mater. 115 (2016) 35–44.
[39] M. Peterlechner et al., Acta Mater. 58 (2010) 6637–6648.
[40] D.C. Hofmann et al., Nature 451 (2008) 1085–1089.
[41] A. Inoue et al., Nat. Mater. 2 (2003) 661–663.
[42] A. Inoue, B.L. Shen, C.T. Chang, Acta Mater. 52 (2004) 4093–4099.
[43] W.H. Wang, C. Dong, C.H. Shek, Mater. Sci. Eng. Res. 44 (2004) 45–89.
[44] S. Pauly et al., Nat. Mater. 9 (2010) 473–477.
[45] Y. Wu et al., Adv. Mater. 22 (2010) 2770–2773.

[46] C. Jeon et al., Acta Mater. 61 (2013) 3012–3026.
[47] D. Xu et al., Acta Mater. 52 (2004) 3493–3497.
[48] Q.K. Jiang et al., Sci. Rep. 2 (2012) 852.
[49] P.J. Jacques et al., Acta Mater. 55 (2007) 3681–3693.
[50] F. Sun et al., Acta Mater. 61 (2013) 6406–6417.
[51] S. Hao et al., ACS Appl. Mater. Interfaces 8 (2016) 2917–2922.
[52] A.C. Larson, R.B. Von Dreele, General Structure Analysis System (GSAS). Los Alamos National Laboratory Report, LAUR 86-748 (2004).
[53] T.C. Hufnagel, R.T. Ott, J. Almer, Phys. Rev. B 73 (2006) 064204.
[54] H.F. Poulsen et al., Nat. Mater. 4 (2005) 33–36.

Supplementary Information

The Supplementary Information includes Table S1 and Fig. S1 to Fig. S17.

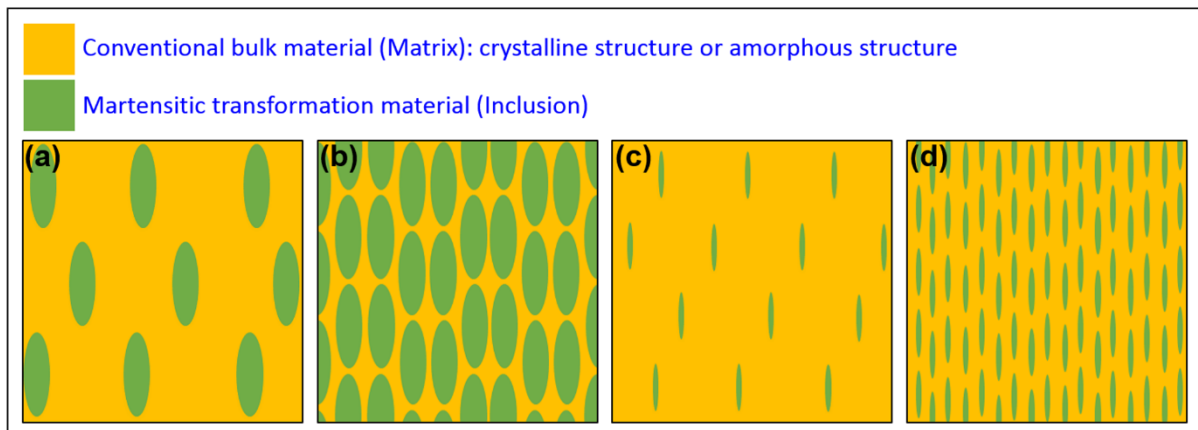## 1. The structural configurations of conventional metal matrix - martensitic transformation metal inclusion composites

Table S1. Classification of conventional bulk matrix - martensitic transformation inclusion composites based on three parameters: matrix structure (M), inclusion size (I), and inclusion spacing (S). The bold **(a)** to **(d)** in the table correspond to the structures presented in **(a)** to **(d)** in Fig. S1.

Matrix structure (M)/ Inclusion size (I)/ Inclusion spacing (S)		Inclusion (Martensitic transformation material) size			
		Coarse		Fine	
		Inclusion spacing		Inclusion spacing	
		Coarse	Fine	Coarse	Fine
Matrix (Conventional bulk material)	Crystalline structure	Crystalline(M)/ Coarse(I)/ Coarse(S) **(a)**	Crystalline(M)/ Coarse(I)/ Fine(S) **(b)**	Crystalline(M)/ Fine(I)/ Coarse(S) **(c)**	Crystalline(M)/ Fine(I)/ Fine(S) **(d)**
	Amorphous structure	Amorphous(M)/ Coarse(I)/ Coarse(S) **(a)**	Amorphous(M)/ Coarse(I)/ Fine(S) **(b)**	Amorphous(M)/ Fine(I)/ Coarse(S) **(c)**	Amorphous(M)/ Fine(I)/ Fine(S) **(d)**

Conventional bulk material (Matrix): crystalline structure or amorphous structure

Martensitic transformation material (Inclusion)

Figure S1. Schematics of structural configurations of conventional metal matrix - martensitic

transformation metal inclusion composites based on two geometrical parameters: inclusion size (I) and inclusion spacing (S). **(a)** Coarse (I)/Coarse (S). **(b)** Coarse (I)/Fine (S). **(c)** Fine (I)/Coarse (S). **(d)** Fine (I)/Fine (S).

Note: The design concept of collective atomic loading is to utilize the uniform lattice strain of the martensitic transformation to stretch the paring conventional material at the atomic level along the interface. In this regard, the microstructure of the conventional material matrix - martensitic transformation inclusion composite may be described using two geometrical parameters: inclusion size (I) and inclusion spacing (S). Based on these two parameters, the various structural configurations of composites can be classified into four basic types, as presented in Table S1 and Fig. S1. The matrix can be either crystalline or amorphous, and of large (coarse) or small (fine) grain size. The martensitic transformation inclusions may be in the forms of particles, rods, discs, wires, ribbons, and lamellae. For simplicity, a prolate ellipsoidal inclusion shape of two different sizes are used to represent the coarse and the fine sized inclusions. The inclusions orientation texture can be isotropic or anisotropic.

High elastic strains may be created locally in the matrix material when the inclusions undergo stress-induced martensitic transformation. Thus, for large inter-inclusion spacing, the martensitic transformation inclusion is unable to penetrate through the matrix and induce large elastic strains in it. This eliminates the validity of the configurations presented in Fig. S1(a) and Fig. S1(c) (the gray and green cells in Table S1). The only options that may have a chance to achieve large global elastic strains in the matrix are those presented in Fig. S1(b) and Fig. S1(d) (the yellow and red cells in Table S1). These two configurations are denoted as

2

coarse(I)/fine(S) and fine(I)/fine(S) structures. However, for the coarse(I)/fine(S) configuration

(Fig. S1(b)), the volume fraction of the matrix is too small. Consequently, the only promising

configuration is the fine(I)/fine(S) structure presented in Fig. S1(d) (the red cell in Table S1).

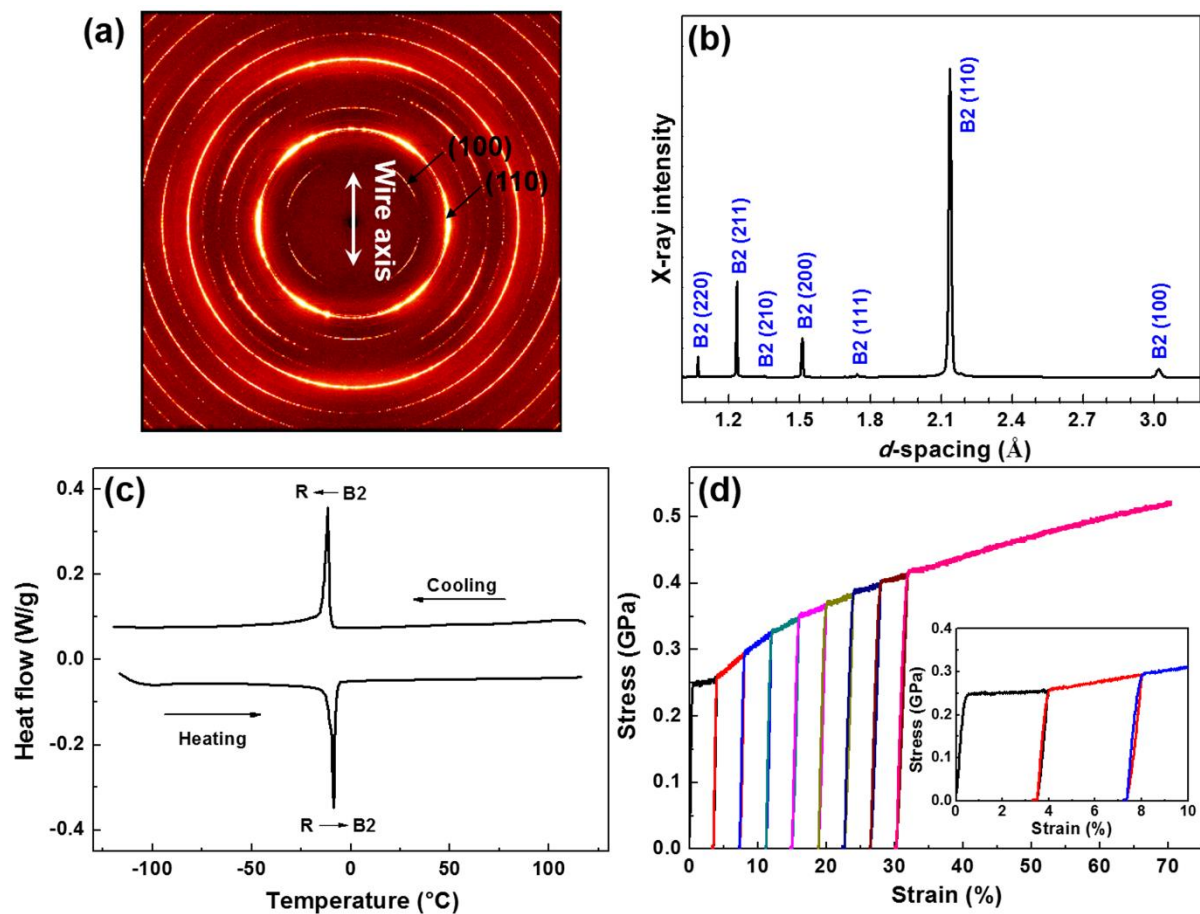## 2. Structures of the amorphous-nanocrystalline composites

Figure S2. The microstructure, phase transformation behavior, and mechanical properties of the Ti$_{50}$Ni$_{47}$Fe$_3$ crystalline wire alloy after annealing at 750 °C. **(a)** Two-dimensional HE-XRD pattern. **(b)** One-dimensional HE-XRD spectrum 360° integrated along the Derby circle of the 2D pattern. **(c)** DSC curve of the wire sample revealing the B2-R phase transformation. **(d)** Room-temperature engineering tensile stress-strain curve of the wire.
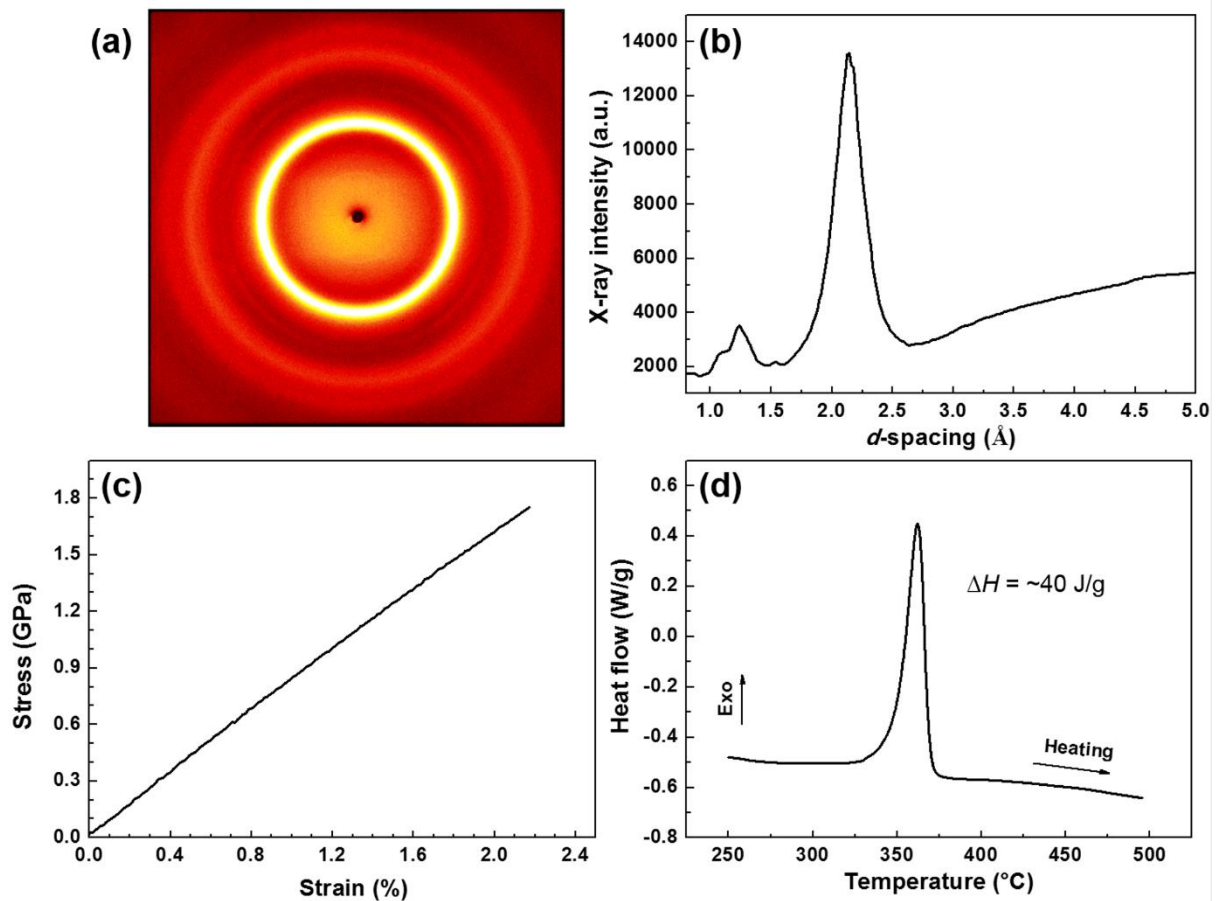
Figure S3. The microstructure, mechanical property and crystallization behavior of the $Ti_{50}Ni_{47}Fe_3$ alloy after full amorphization by severe cold wire drawing. **(a)** Two-dimensional HE-XRD pattern demonstrating the fully amorphous state. **(b)** 360° integrated one-dimensional HE-XRD spectrum. **(c)** Room-temperature engineering tensile stress-strain curve. **(d)** DSC heating curve of the amorphous wire sample revealing the crystallization behavior.
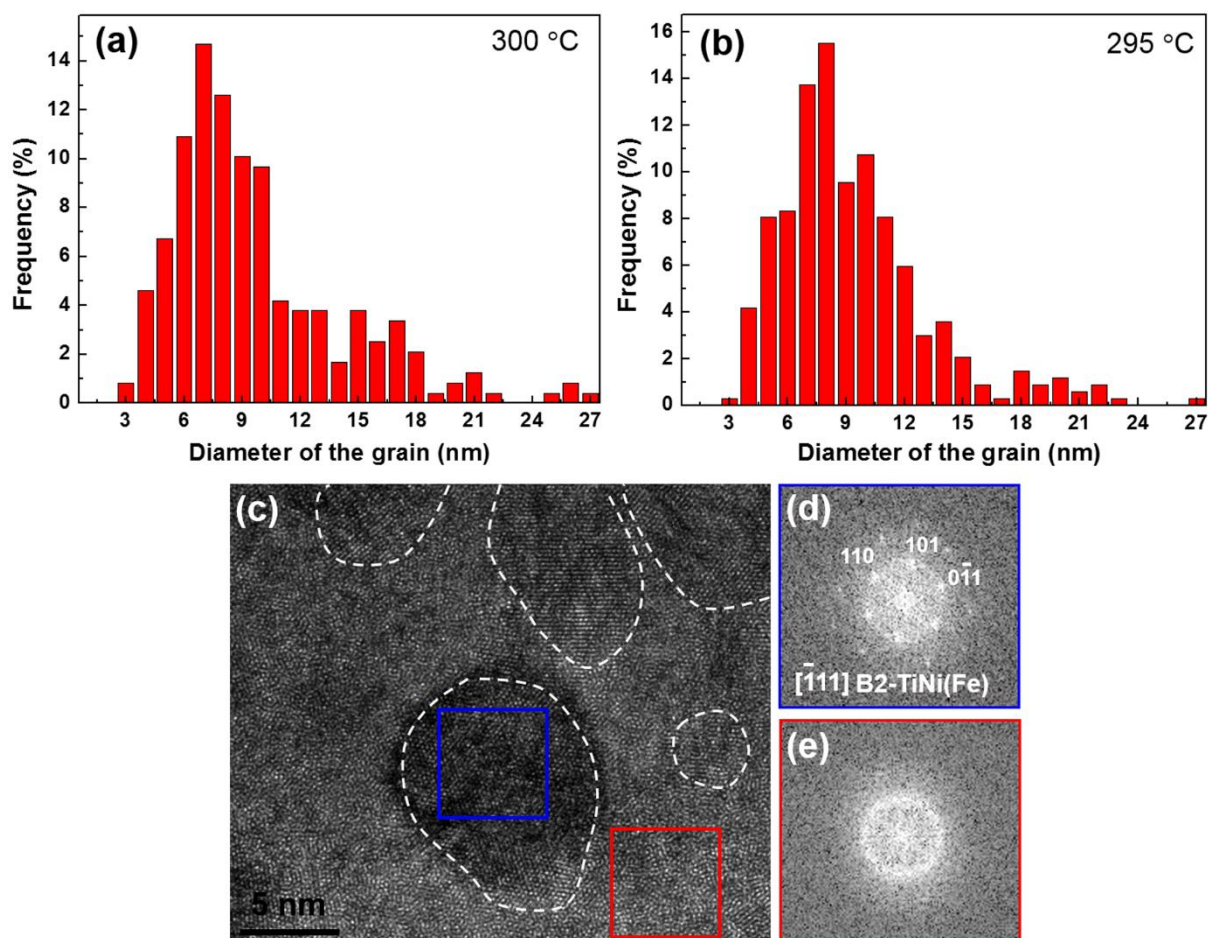
Figure S4. The microstructure of in-situ amorphous-nanocrystalline composites. **(a, b)** Grain size distributions in the 300 °C and 295 °C annealed composites, respectively. The average grain size of the nanocrystalline is 9.7 nm in the 300 °C annealed sample and 9.4 nm in the 295 °C annealed sample. **(c)** HRTEM micrograph of the 295 °C annealed composite. **(d, e)** FFT patterns of the nanocrystalline region (blue frame) and the amorphous matrix (red frame), respectively, shown in (c).
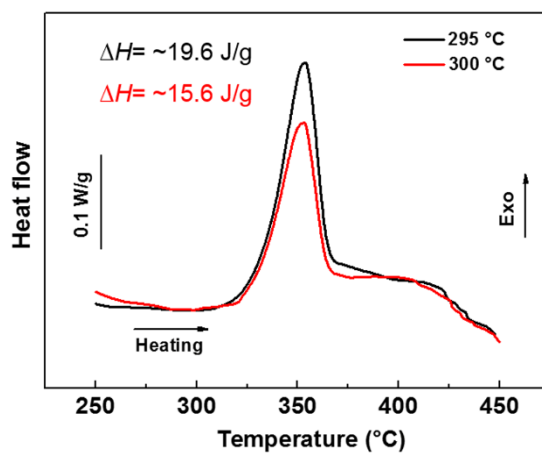
Figure S5. DSC curves of the crystallization behavior of the in-situ amorphous-nanocrystalline

composites. The volume fraction of the amorphous matrix in the 300 °C and 295 °C annealed samples are estimated to be 39% and 49%, respectively, based on the value of the exothermic heat relative to that of the fully amorphous sample shown in Fig. S3(d).
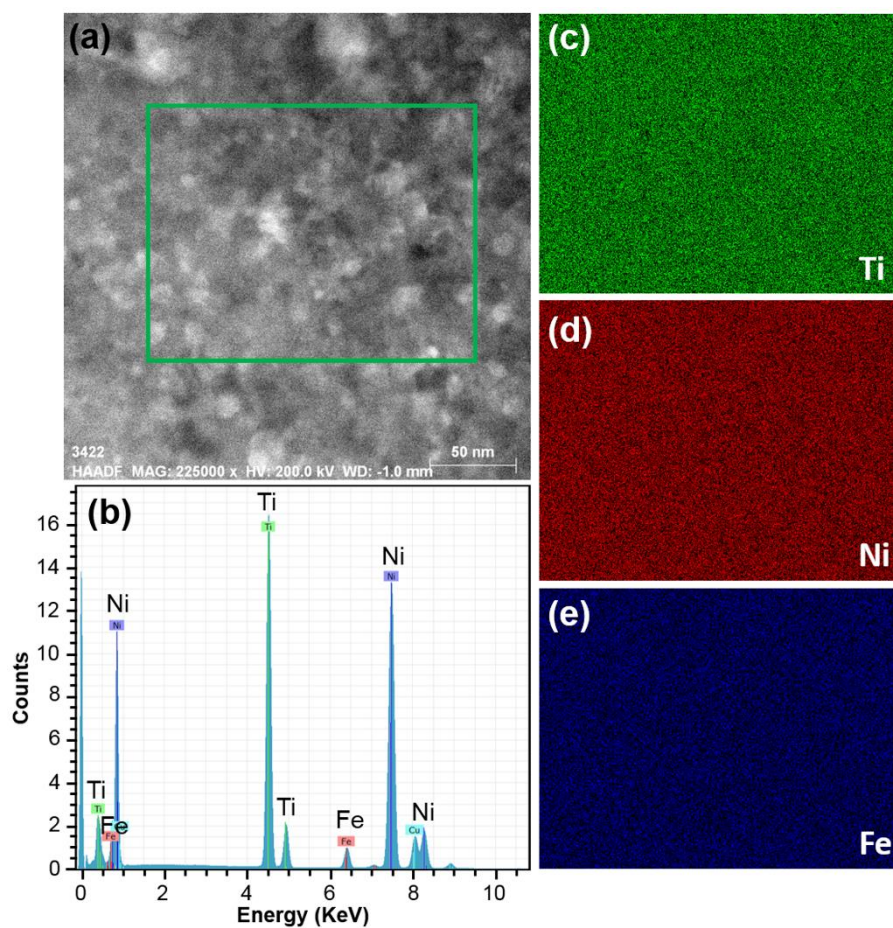
Figure S6. Energy dispersive X-ray spectrometry analysis of the chemical composition distribution of the 300 °C annealed composite. **(a)** Scanning transmission electron microscopy image. **(b)** Energy dispersive X-ray spectrum. The copper is from TEM grid. **(c, d, e)** Elemental mapping of Ti, Ni and Fe, respectively, indicating uniform composition distribution of the annealed sample.
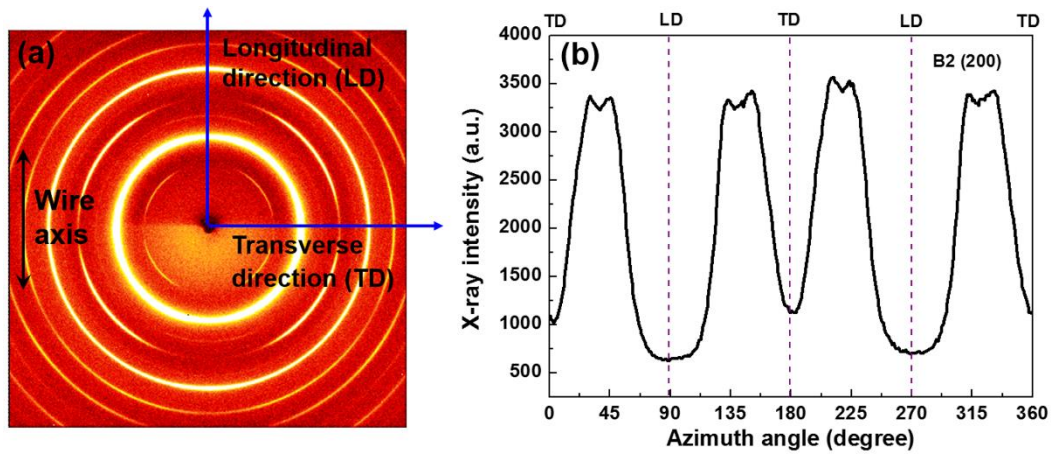
Figure S7. Synchrotron high energy XRD analysis of the structure and texture of the TiNiFe in-situ composites. **(a)** Two-dimensional HE-XRD pattern of the 300 °C annealed composite. **(b)** B2-TiNi(Fe) (200) diffraction intensity distribution along the azimuth circle revealing the orientation texture of the nanocrystalline domains with their [100] direction oriented at 50° from the wire axial direction or longitudinal direction.

3. Mechanical properties of the amorphous-nanocrystalline composites
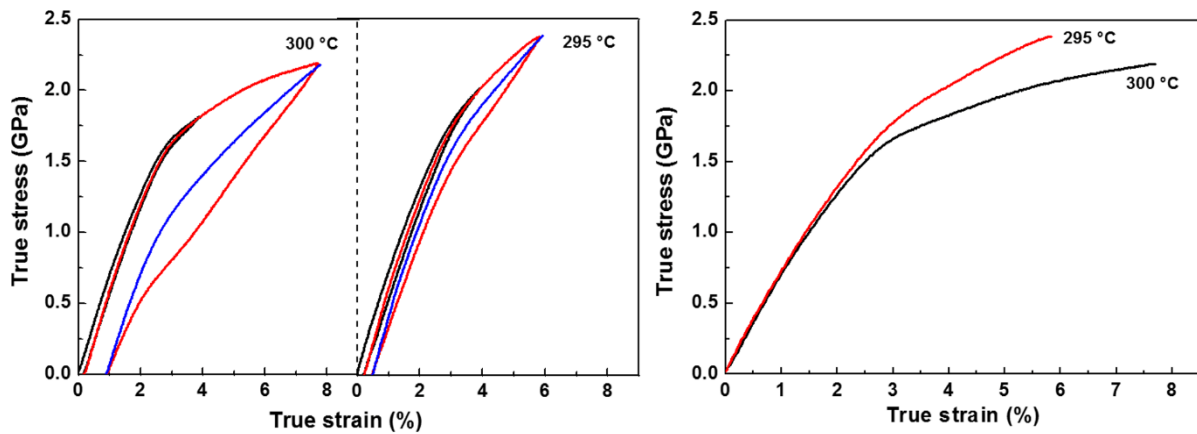
Figure S8. Room-temperature true tensile stress-strain curves of the 300 °C and 295 °C annealed composites. **(a)** Cyclic loading-unloading. **(b)** One-time loading.
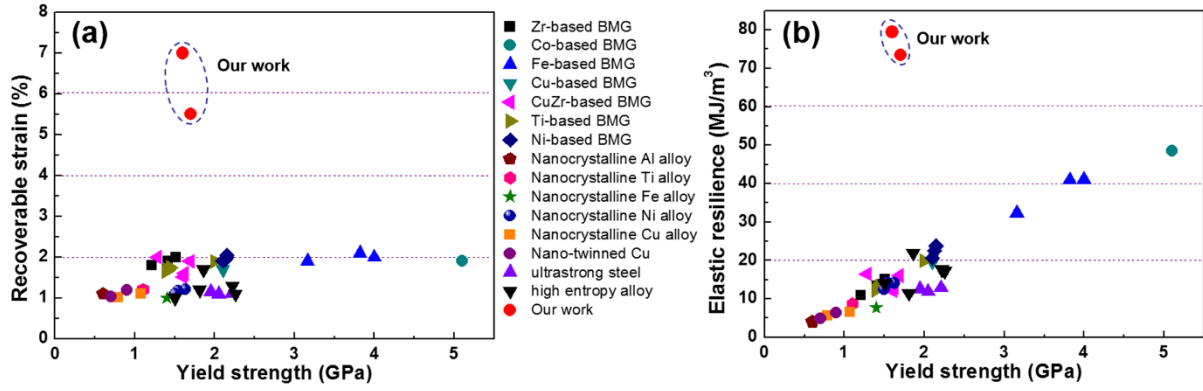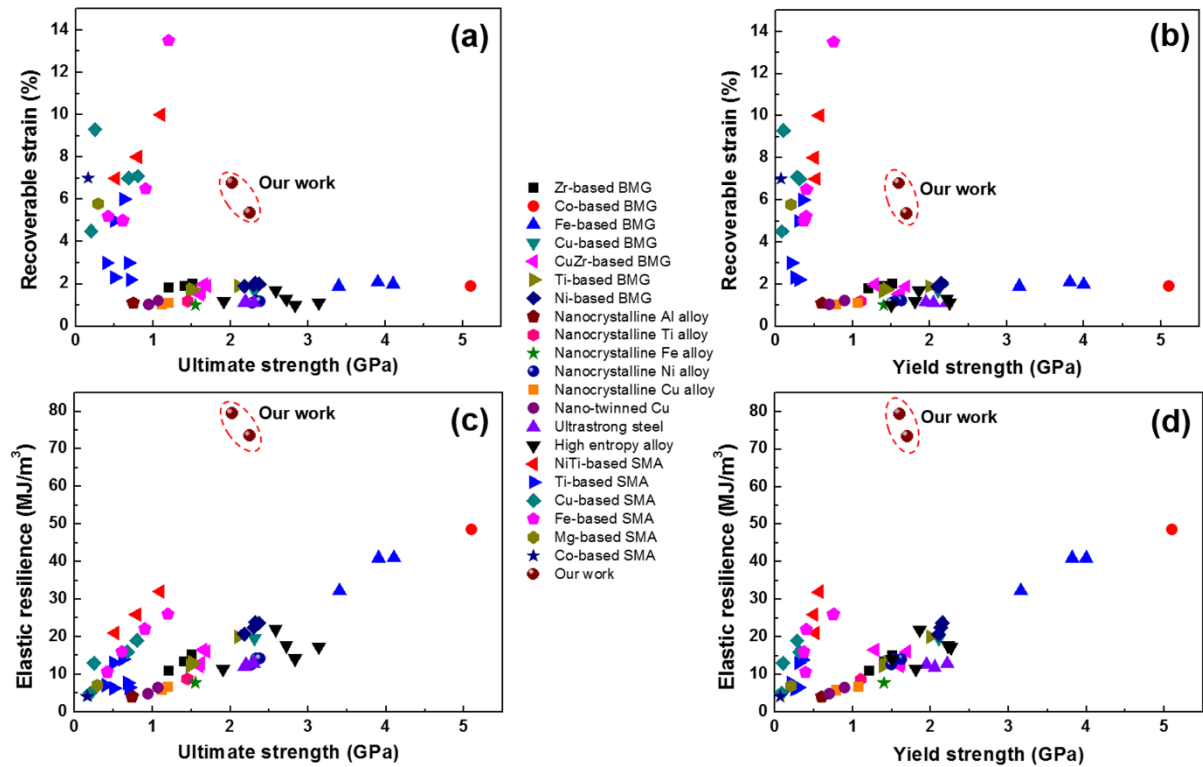
Figure S9. Comparison of the mechanical properties of our in-situ amorphous-nanocrystalline composites with those of other existing high strength bulk metallic materials. **(a)** Comparison of the recoverable strain and yield strength. **(b)** Comparison of the elastic resilience and yield strength. These existing high strength bulk metallic materials include Zr-based bulk metallic glass (BMG)[40], Co-based BMG[41], Fe-based BMG[42], Cu-based BMG[11,43], CuZr-based BMG[44,45], Ti-based BMG[46], Ni-based BMG[47], nanocrystalline Al alloy[22], nanocrystalline Ti alloy[23], nanocrystalline Fe alloy[24], nanocrystalline Ni alloy[25], nanocrystalline Cu alloy[26], nano-twinned Cu[21], ultrastrong steel[18,27], and high entropy alloy[20,28].

Figure S10. Comparison of mechanical properties of our in-situ amorphous-nanocrystalline composites

with those of other existing high strength bulk metallic materials and common shape memory alloys (SMAs). **(a)** Comparison of the recoverable strain and ultimate strength. **(b)** Comparison of the recoverable strain and yield strength. **(c)** Comparison of the elastic resilience and ultimate strength. **(d)** Comparison of the elastic resilience and yield strength. These existing high strength bulk metallic materials include Zr-based bulk metallic glass (BMG)[40], Co-based BMG[41], Fe-based BMG[42], Cu-based BMG[11,43], CuZr-based BMG[44,45], Ti-based BMG[46], Ni-based BMG[47], nanocrystalline Al alloy[22], nanocrystalline Ti alloy[23], nanocrystalline Fe alloy[24], nanocrystalline Ni alloy[25], nanocrystalline Cu alloy[26], nano-twinned Cu[21], ultrastrong steel[18,27], and high entropy alloy[20,28]. The common SMAs include NiTi-based SMAs[36,55,56], Ti-based SMAs[57-62], Cu-based SMAs[63-66], Fe-based SMAs[67-70], Mg-based SMAs[71], and Co-based SMAs[72].

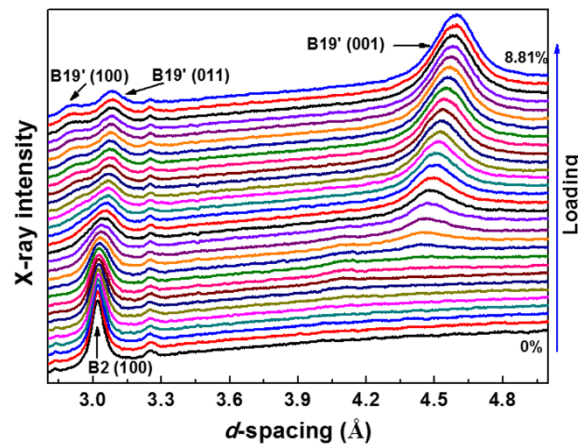## 4. In-situ synchrotron HE-XRD analysis of the amorphous-nanocrystalline composites

Figure S11. Full azimuthal circle (0° to 360°) integrated one-dimensional HE-XRD spectrums of the 300 °C annealed composite during tensile deformation. The appearance and heightening of the B19' diffraction peaks and the diminishing of the B2 diffraction peaks indicate the stress induced B2→B19' transformation of the nanocrystalline domains.
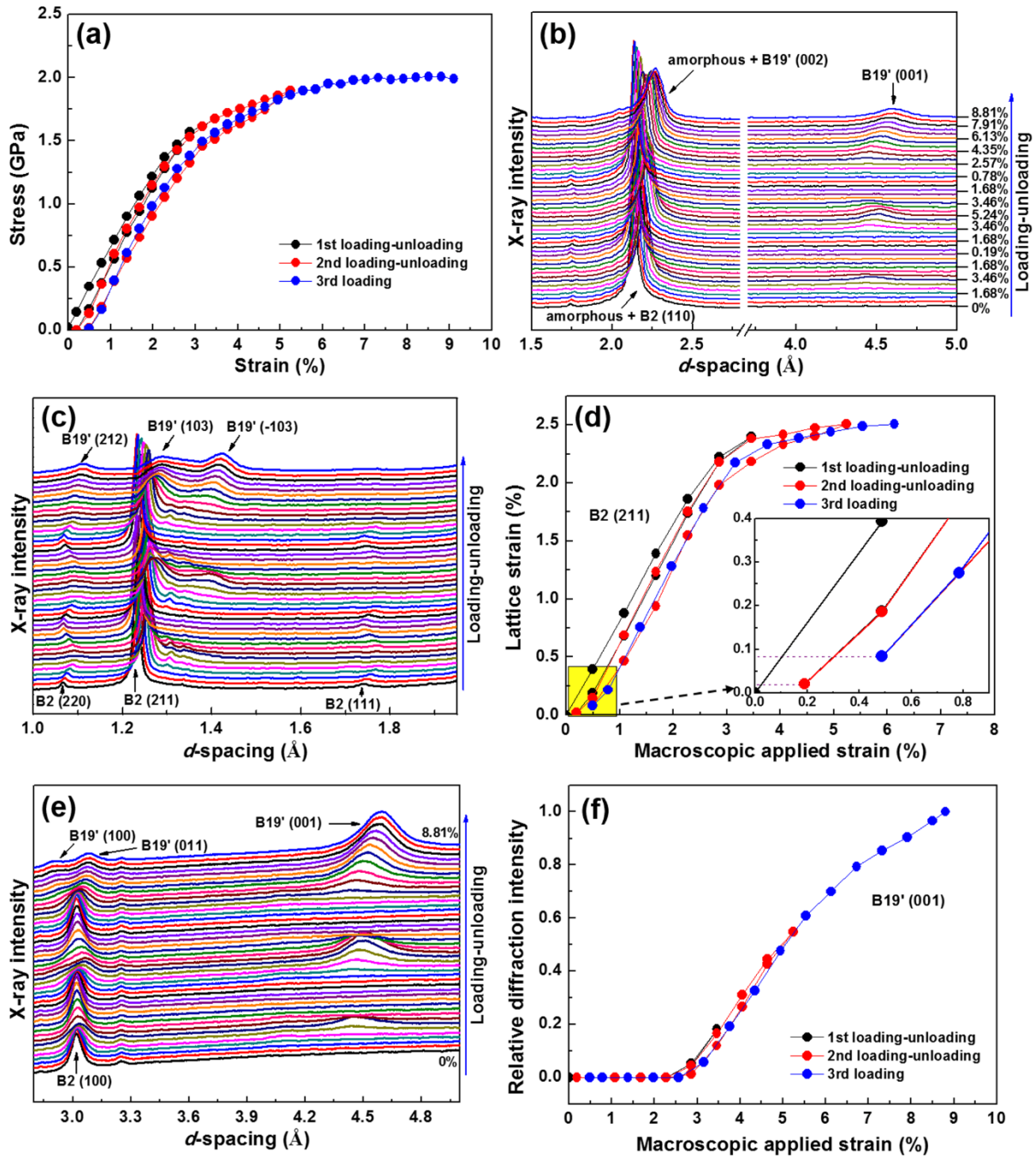
Figure S12. In-situ synchrotron HE-XRD analysis of the 300 °C annealed composite during cyclic tensile deformation. **(a)** Room-temperature engineering tensile stress-strain curves of the composite over three deformation cycles. **(b, c)** One-dimensional HE-XRD spectrums of the composite during cyclic tensile deformation in the loading direction. **(d)** Evolution of the lattice strain of austenite B2 (211) in the loading direction as functions of the applied macroscopic strain. The inset shows an enlarge view of the lattice strain curve of the B2 (211) in the yellow area. **(e)** Full azimuthal circle (0° to 360°) integrated one-dimensional HE-XRD spectrums of the composite during the cyclic tensile deformation. **(f)** Evolution of the relative intensity of the martensite B19' (001) diffraction peak during the cyclic

tensile deformation. The relative intensity is defined as the ratio of the integrated area of the martensite B19' (001) diffraction peak at a given applied macroscopic strain to that of the martensite B19' (001) diffraction peak at the maximum applied strain.

Note: It is seen in Fig. S12(b), Fig. S12(c), Fig. S12(e) and Fig. S12(f) that upon unloading, the austenite B2-TiNi(Fe) phase underwent a fully reverse transformation from the stress-induced martensite B19' to the austenite B2 phase. After unloading, the B2-TiNi(Fe) nanocrystalline phase sustained an elastic tensile strain. This microscopic elastic tensile strain increased with increasing the macroscopic tensile cycle strain (Fig. S12(d)). The tensile lattice strain after the deformation cycle implies that plastic deformation has occurred in the amorphous matrix during the deformation cycle, which caused the macroscopic residual strain of the composite after unloading.
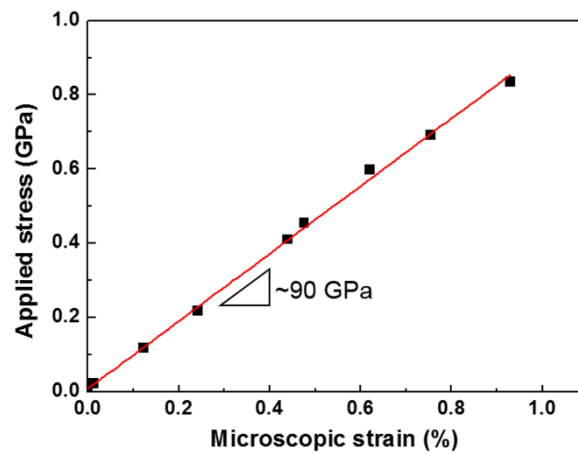

Figure S13. Evolution of the microscopic strain of fully amorphous TiNiFe alloy in the loading direction as functions of the applied macroscopic stress. The modulus of amorphous TiNiFe alloy is estimated to be 90 GPa based on the slope of the applied stress-microscopic strain curve.

5. Further experiments to verify the hypothesis

Experiment 1: Decreasing the phase transformation temperature

Increasing Fe content from 3 to 4.5 at. % lowers the martensitic transformation temperature, thus making the stress-induced martensitic transformation at the room temperature more difficult and incomplete. As seen in Fig. S14 below, the composite becomes more brittle with a maximum macroscopic strain of 4%, apparently due to the weakened effect of collective atomic loading from the reduced martensitic transforming domains.
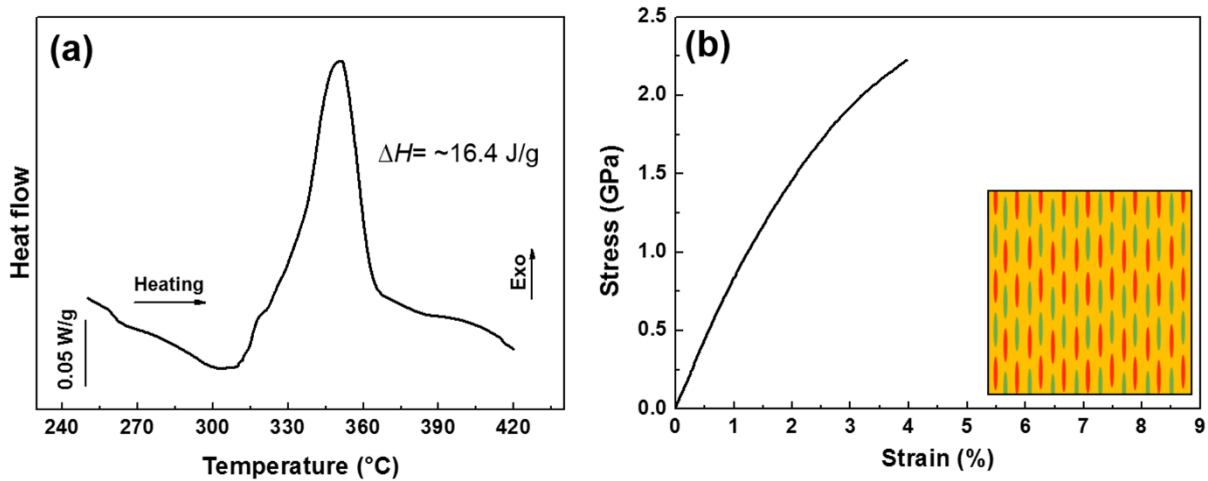

Figure S14. Mechanical properties of $Ti_{50}Ni_{45.5}Fe_{4.5}$ (at. %) amorphous-nanocrystalline composite annealed at 290 °C for 10 min. **(a)** DSC curve on heating of the composite, revealing the crystallization of the amorphous matrix, based on which the volume fraction of the amorphous matrix in this composite is estimated to be 41%. **(b)** Engineering tensile stress-strain curve tested at the room temperature. The inset is a schematic of the composite configuration and the occurrence of stress induced martensitic transformation in the nanocrystalline inclusions, with the green color represents martensitic transformation and red color indicates no martensitic transformation.

Experiment 2: Increasing testing temperature

By increasing the testing temperature, the stress-induced martensitic transformation in the

nanocrystalline domains is reduced and eventually suppressed completely. It is evident below that this leads to a gradual reduction of the maximum strain the composite is able to sustain before rupture.
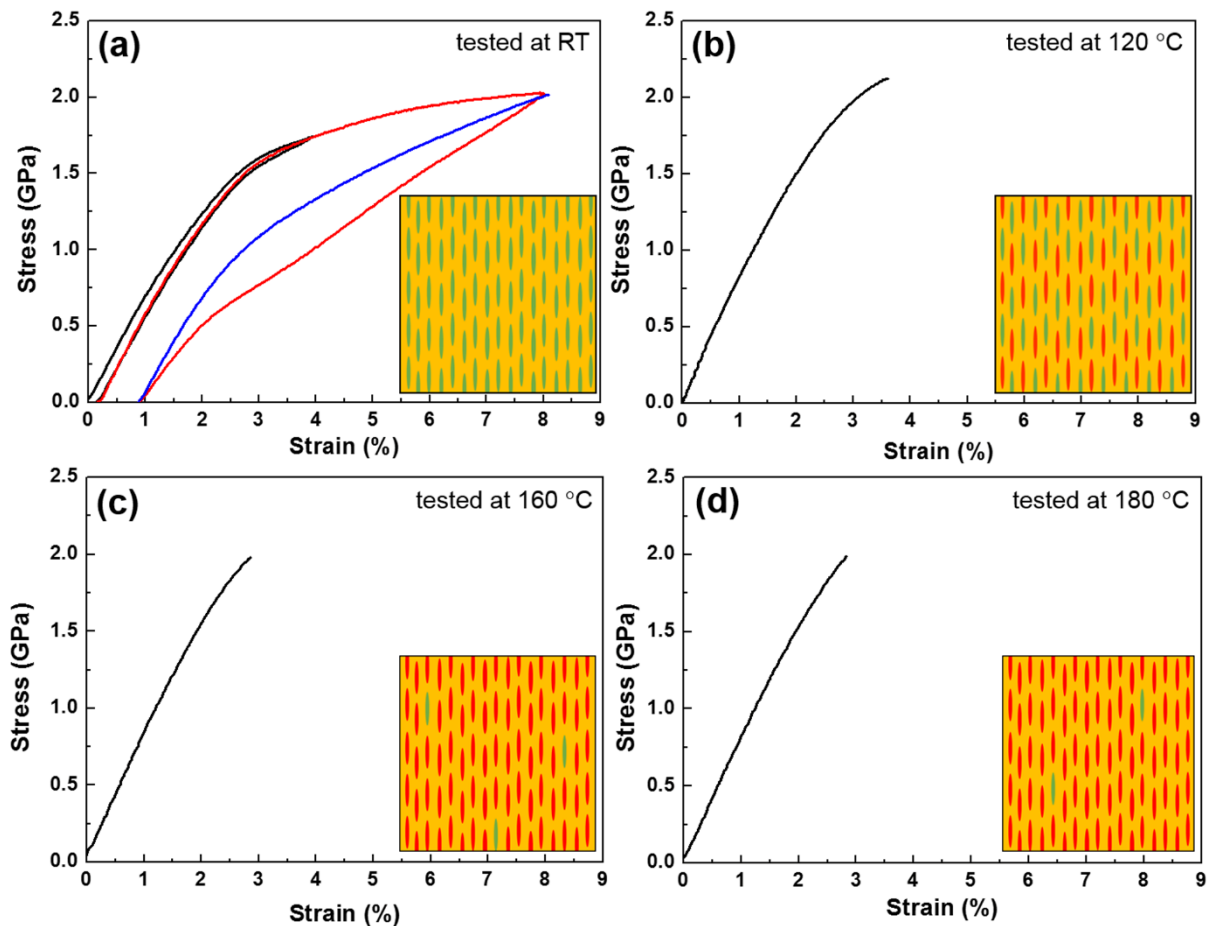

Figure S15. Engineering tensile stress-strain curves of the 300 °C annealed composite tested at different temperatures. **(a)** RT. **(b)** 120 °C. **(c)** 160 °C. **(d)** 180 °C. The insets show schematics of the occurrence of the stress-induced martensitic transformation in the nanocrystalline domains, with the green color represents martensitic transformation and red color indicates no martensitic transformation.

Experiment 3: Reducing the volume fraction of the nanocrystalline phase

The volume fraction (and size) of the nanocrystalline domains can be reduced by lowering the crystallization annealing temperature. It is seen in the evidence below that by lowering the

annealing temperature to 290 °C, the maximum macroscopic strain of the composite is reduced

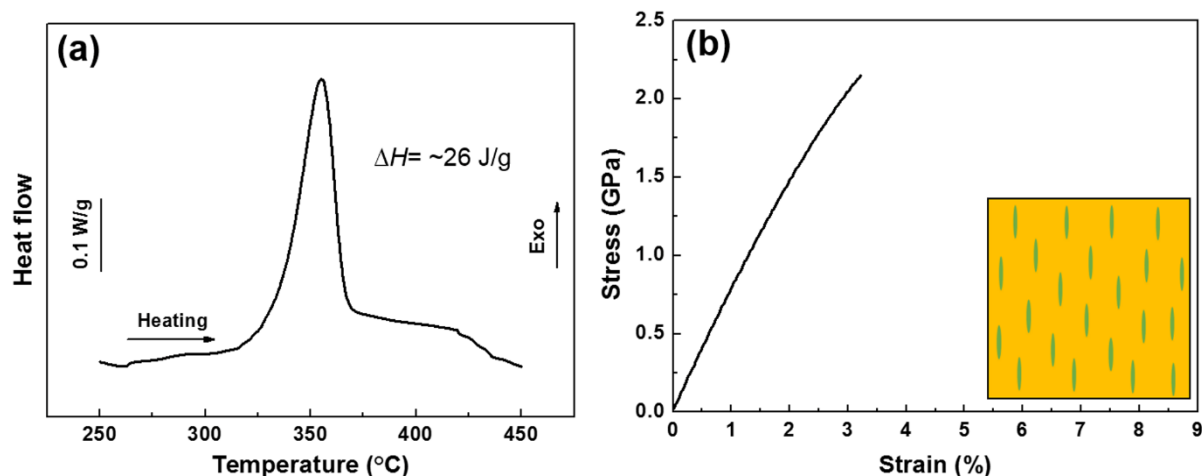to 3.25%, due to the weakened effect of collective atomic loading.

Figure S16. Mechanical behavior of a 290 °C annealed composite. **(a)** DSC heating curve of the 290 °C annealed sample, revealing the crystallization of the amorphous matrix. Based on this the volume fraction of the amorphous matrix is estimated to be 65% (i.e. less nanocrystalline domains). **(b)** Room-temperature engineering tensile stress-strain curve. The inset shows a schematic of then low density nanocrystalline inclusions in the composite.
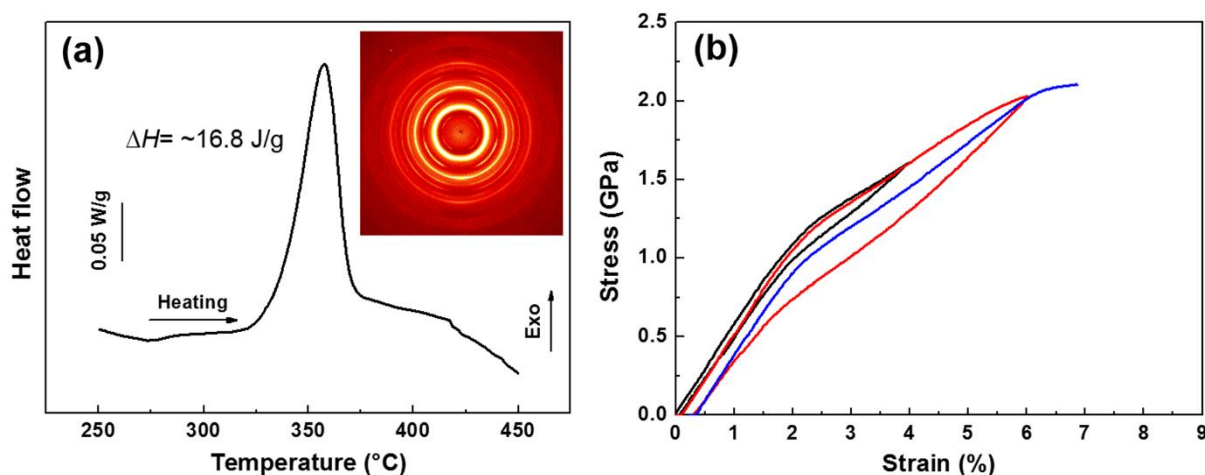

Figure S17. The crystallization behavior, microstructure, and mechanical properties of $Ti_{50}Ni_{50}$ (at. %) amorphous-nanocrystalline composite annealed at 290 °C for 10 min. **(a)** DSC curve on heating of the composite, revealing the crystallization of the amorphous matrix, based on which the volume fraction

of the amorphous matrix in this composite is estimated to be 42%. The inset shows its corresponding two-dimensional HE-XRD pattern. **(b)** Room-temperature engineering tensile stress-strain curve.

Note: Decreasing Fe content from 3 to 0 at% raises the martensitic transformation temperature, thus making the stress-induced martensitic transformation at the room temperature easier, which results in the reduced yield strength of the composite.

55. Tan, S. M. & Miyazaki, S. Ti-content dependence of transformation pseudoelasticity characteristics of Ti$_x$Ni$_{(92-x)}$Cu$_8$ shape memory alloys. *Mater. Sci. Eng. A* **237**, 79-86 (1997).

56. Liu, Y., Houver, I., Xiang, H., Bataillard, L. & Miyazaki, S. Strain dependence of pseudoelastic hysteresis of NiTi. *Metall. Mater. Trans. A* **30**, 1275-1282 (1999).

57. Takahashi, E., Sakurai, T., Watanabe, S., Masahashi, N. & Hanada, S. Effect of heat treatment and Sn content on superelasticity in biocompatible TiNbSn alloys. *Mater. Trans.* **43**, 2978-2983 (2002).

58. Fukui, Y., Inamura, T., Hosoda, H., Wakashima, K. & Miyazaki, Shuichi. Mechanical properties of a Ti-Nb-Al shape memory alloy. *Mater. Trans.* **45**, 1077-1082 (2004).

59. Maeshima, T., Ushimaru, S., Yamauchi, K. & Nishida, M. Effects of Sn content and aging conditions on superelasticity in biomedical Ti-Mo-Sn alloys. *Mater. Trans.* **47**, 513-517 (2006).

60. Tomio, Y., Furuhara, T. & Maki, Tadashi. Effect of cooling rate on superelasticity and microstructure evolution in Ti-10V-2Fe-3Al and Ti-10V-2Fe-3Al-0.2N alloys. *Mater. Trans.* **50**, 2731-2736 (2009).

61. Kim, H. Y., Ikehara, Y., Kim, J. I., Hosoda, H. & Miyazaki, S. Martensitic transformation, shape memory effect and superelasticity of Ti-Nb binary alloys. *Acta Mater.* **54**, 2419-2429 (2006).

62. Pavón, L. L., Kim, H. Y., Hosoda, H. & Miyazaki. S. Effect of Nb content and heat treatment temperature on superelastic properties of Ti-24Zr-(8-12)Nb-2Sn alloys. *Scr. Mater.* **95**, 46-49 (2015).

63. Sutou, Y., Omori, T., Kainuma, R. & Ishida, K. Ductile Cu-Al-Mn based shape memory alloys: general properties and applications. *Mater. Sci. Tech.* **24**, 896-901 (2008).

64. Sutou, Y., Omori, T., Kainuma, R. & Ishida, K. Grain size dependence of pseudoelasticity in polycrystalline Cu-Al-Mn-based shape memory sheets. *Acta Mater.* **61**, 3842-3850 (2013).

65. Sutou, Y. *et al*. Effect of grain size and texture on pseudoelasticity in Cu-Al-Mn-based shape memory wire. *Acta Mater.* **53,** 4121-4133 (2005).

66. Somerday, M., Wert, J. A. & Comstock. R. J. Effect of grain size on the observed pseudoelastic behavior of a Cu-Zn-Al shape memory alloy. *Metall. Mater. Trans. A* **28**, 2335-2341 (1997).

67. Omori, T. *et al*. Superelastic effect in polycrystalline ferrous alloys. *Science* **333**, 68-71 (2011).

68. Tanaka, Y. *et al*. Ferrous polycrystalline shape-memory alloy showing huge superelasticity. *Science* **327**, 1488-1490 (2010).

69. Lee, D., Omori, T. & Kainuma, R. Ductility enhancement and superelasticity in Fe-Ni-Co-Al-Ti-B polycrystalline alloy. *J. Alloy. Compd.* **617**, 120-123 (2014).

70. Omori, T. *et al*. Thermoelastic martensitic transformation and superelasticity in Fe-Ni-Co-Al-Nb-B polycrystalline alloy. *Scr. Mater.* **69**, 812-815 (2013).

71. Ogawa, Y., Ando, D., Sutou, Y. & Koike, J. A lightweight shape-memory magnesium alloy. *Science* **353**, 368-370 (2016).

72. Tanaka, Y. *et al*. Martensitic transition and superelasticity of Co-Ni-Al ferromagnetic shape memory alloys with β+γ two-phase structure. *Mater. Sci. Eng. A* **438**, 1054-1060 (2006).